



## Virtual histology of an entire mouse brain from formalin fixation to paraffin embedding. Part 1: Data acquisition, anatomical feature segmentation, tracking global volume and density changes

Griffin Rodgers<sup>a,b</sup>, Willy Kuo<sup>c,d</sup>, Georg Schulz<sup>a,b</sup>, Mario Scheel<sup>e</sup>, Alexandra Migga<sup>a,b</sup>, Christos Bikis<sup>a,b,f</sup>, Christine Tanner<sup>a,b,\*</sup>, Vartan Kurtcuoglu<sup>c,d</sup>, Timm Weitkamp<sup>e</sup>, Bert Müller<sup>a,b</sup>

<sup>a</sup> Biomaterials Science Center, Department of Biomedical Engineering, University of Basel, 4123 Allschwil, Switzerland

<sup>b</sup> Biomaterials Science Center, Department of Clinical Research, University Hospital Basel, 4031 Basel, Switzerland

<sup>c</sup> The Interface Group, Institute of Physiology, University of Zurich, 8057 Zurich, Switzerland

<sup>d</sup> National Centre of Competence in Research, Kidney.CH, 8057 Zurich, Switzerland

<sup>e</sup> Synchrotron Soleil, 91192 Gif-sur-Yvette, France

<sup>f</sup> Integrierte Psychiatrie Winterthur – Zürcher Unterland, 8408 Winterthur, Switzerland

### ARTICLE INFO

#### Keywords:

Hard X-ray computed tomography  
Synchrotron radiation-based microtomography  
Virtual histology  
Ethanol dehydration  
Paraffin embedding  
Volume shrinkage

### ABSTRACT

**Background:** Micrometer-resolution neuroimaging with gold-standard conventional histology requires tissue fixation and embedding. The exchange of solvents for the creation of sectionable paraffin blocks modifies tissue density and generates non-uniform brain shrinkage.

**New method:** We employed synchrotron radiation-based X-ray microtomography for slicing- and label-free virtual histology of the mouse brain at different stages of the standard preparation protocol from formalin fixation via ascending ethanol solutions and xylene to paraffin embedding. Segmentation of anatomical regions allowed us to quantify non-uniform tissue shrinkage. Global and local changes in X-ray absorption gave insight into contrast enhancement for virtual histology.

**Results:** The volume of the entire mouse brain was 60%, 56%, and 40% of that in formalin for, respectively, 100% ethanol, xylene, and paraffin. The volume changes of anatomical regions such as the hippocampus, anterior commissure, and ventricles differ from the global volume change. X-ray absorption of the full brain decreased, while local absorption differences increased, resulting in enhanced contrast for virtual histology. These trends were also observed with laboratory microtomography measurements.

**Comparison with existing methods:** Microtomography provided sub-10  $\mu\text{m}$  spatial resolution with sufficient density resolution to resolve anatomical structures at each step of the embedding protocol. The spatial resolution of conventional computed tomography and magnetic resonance microscopy is an order of magnitude lower and both do not match the contrast of microtomography over the entire embedding protocol. Unlike feature-to-feature or total volume measurements, our approach allows for calculation of volume change based on segmentation.

**Conclusion:** We present isotropic micrometer-resolution imaging to quantify morphology and composition changes in a mouse brain during the standard histological preparation. The proposed method can be employed to identify the most appropriate embedding medium for anatomical feature visualization, to reveal the basis for the dramatic X-ray contrast enhancement observed in numerous embedded tissues, and to quantify morphological changes during tissue fixation and embedding.

\* Corresponding author at: Biomaterials Science Center, Department of Biomedical Engineering, University of Basel, 4123 Allschwil, Switzerland.

E-mail address: [christine.tanner@unibas.ch](mailto:christine.tanner@unibas.ch) (C. Tanner).

<sup>1</sup> [www.bmc.unibas.ch](http://www.bmc.unibas.ch)

<https://doi.org/10.1016/j.jneumeth.2021.109354>

Received 15 July 2021; Received in revised form 1 September 2021; Accepted 4 September 2021

Available online 13 September 2021

0165-0270/© 2021 The Authors. Published by Elsevier B.V. This is an open access article under the CC BY license (<http://creativecommons.org/licenses/by/4.0/>).

## 1. Introduction

The micro- and nano-morphology of the neuronal network is closely related to brain function. Therefore, (sub-)cellular imaging plays a crucial role in understanding the brain in health and disease. The gold standard for sub-micrometer histological analysis involves tissue fixation, embedding, sectioning, staining, and imaging with light or electron microscopy (Culling, 1974). Benefits of optical microscopy include fast imaging in two dimensions and well-established histochemical staining protocols for function-related contrast and differentiation of anatomical features. A drawback is that physical slicing is irreversible and introduces artifacts (Pichat et al., 2018; Germann et al., 2008). Volumetric histological imaging relies on serial sectioning, which typically provides anisotropic spatial resolution limited by the section thickness and true micrometer resolution is time consuming (Amunts et al., 2013; Gong et al., 2013).

Thanks to the penetration of hard X-rays through matter, microtomography offers a complementary three-dimensional neuroimaging approach that generates isotropic micrometer resolution without serial sectioning. The X-ray absorption of soft tissues is weak, which is why microtomography of brain tissue has traditionally relied on contrast agents. Staining for cells with heavy metal compounds such as silver nitrate has allowed for impressive visualization of the cytoarchitecture of the brain (Mizutani et al., 2008; Mizutani and Suzuki, 2012). Many protocols have been suggested including osmium-based (Böhm et al., 2019; Barbone et al., 2020), iodine-based (Anderson and Maga, 2015; Saccomano et al., 2018), and Golgi-Cox mercury-based impregnation (Fonseca et al., 2018; Jiang et al., 2021). Unfortunately, selection and usage of X-ray contrast agents is sample- and target-specific, hence presenting a barrier for non-experts.

X-ray phase contrast methods at synchrotron radiation facilities offer higher density resolution than absorption contrast (Momose, 2005), allowing for imaging of the minute native density differences in brain tissue without staining (Schulz et al., 2010; Pinzer et al., 2012). This has enabled label-free imaging of cyto- and angioarchitecture of whole rodent brains (Zhang et al., 2015; Barbone et al., 2018). It has also been used for the quantitative analysis of cytoarchitecture within neuronal volumes up to tens of  $\text{mm}^3$  in size for mice and humans (Dyer et al., 2017; Hieber et al., 2016; Töpperwien et al., 2018). Unique possibilities such as capillary-level visualization of amyloid-angiopathy were demonstrated in a mouse brain model of Alzheimer's disease (Massimi et al., 2019). Advances in computing power and acquisition techniques have allowed for imaging of the full mouse brain at around  $1 \mu\text{m}$  resolution, though the related datasets are not thoroughly presented in the literature (Vescovi, 2018; Miettinen et al., 2019). These developments are contributing to the rise of X-ray virtual histology (Albers et al., 2018a), which can complement standard histology as part of a multimodal imaging strategy (Uludağ and Roebroek, 2014; Katsamenis et al., 2019). Still, the limited accessibility of synchrotron radiation sources prevents more widespread use. Recently, state-of-the-art laboratory X-ray sources have demonstrated promising results for virtual histology (Albers et al., 2018b; Vågberg et al., 2018; Busse et al., 2018; Zdora et al., 2020) including cellular-resolution neuroimaging (Töpperwien et al., 2018; Töpperwien and van der Meer, 2020), but these systems are still not commonplace.

Fortunately, the modified electron density of brain tissue fixed in ethanol or embedded in paraffin (Töpperwien et al., 2019) allows for the use of conventional laboratory-based absorption-contrast systems for virtual histology (Khimchenko et al., 2016). Paraffin embedding is used in standard histology, meaning well-established preparation protocols exist and virtual histology can be incorporated into the workflow of conventional histology. This allows for validation of virtual histology with well-selected histochemical stains (Töpperwien and van der Meer, 2020) and extension of conventional histology to the third dimension with slice-to-volume registration (Khimchenko et al., 2016; Chicherova et al., 2018). Thus, paraffin embedding is becoming increasingly popular

among the X-ray imaging community, even for imaging beyond the optical limit (Khimchenko et al., 2018; Kuan et al., 2020).

Each step of the paraffin embedding protocol introduces significant tissue shrinkage. This effect is well known, but quantification of shrinkage has previously been based on length measurements of dissected tissue (Quester and Schröder, 1997). Volume change measurements based on computed tomography and magnetic resonance imaging (MRI) have been reported (Wehrl et al., 2015), however higher spatial and density resolution are needed for the quantification of morphology change of smaller anatomical regions within the brain.

The objective of this two-part study is to quantify morphological and density changes within the mouse brain as a result of tissue embedding. To this end, we employ synchrotron radiation-based X-ray micro computed tomography to visualize an entire mouse brain over the course of paraffin embedding, i.e. in formalin, five ascending ethanol solutions (50%, 70%, 80%, 90%, and 100%), xylene, and finally paraffin; see Fig. 1 for the workflow. In this Part 1 manuscript, we report the brain preparation, image acquisition procedure, and semi-automatic segmentation of anatomical features before describing the measured changes in volume and density of selected anatomical regions. Part 2 of this publication (Rodgers et al., 2021a) provides details and validation of the image registration method which is used to extract volumetric strain fields, and reports on the local volume and contrast changes.

## 2. Materials and methods

### 2.1. Mouse brain extraction and preparation

All tissue collected in this study was excess material from an experiment approved by the veterinary office of the Canton of Zurich (license number ZH067/17). The brain of one six-month-old female C57BL/6Jrj mouse (Janvier Labs, Le Genest-Saint-Isle, France) was extracted and immersion-fixed with 4% formaldehyde / phosphate buffered saline after sacrifice. The standard paraffin embedding protocol was used (Wolfe, 2019): after immersion in 4% formaldehyde/phosphate buffered saline (Sigma Aldrich, Darmstadt, Germany/Thermo Fisher Scientific, Massachusetts, USA), the brain was immersed for two hours in each of 50%, 70%, 80%, 90%, and 100% ethanol solutions, xylene (20 mL each, Carl Roth GmbH, Karlsruhe, Germany). Finally, the sample was transferred to liquid paraffin wax (ROTI® Plast, Carl Roth GmbH, Karlsruhe, Germany) for two hours, then cooled to form a solid paraffin block.

Between each step, the sample was transferred to a 1.5 mL Eppendorf tube and scanned while immersed in the specific embedding medium. The solidified paraffin block was trimmed to remove excess material and directly glued to the sample holder for tomographic measurement. Fig. 1 shows a sketch of the sequence of sample preparation and experimental set-up.

### 2.2. Synchrotron radiation-based X-ray microtomography

Microtomography measurements were performed at the ANATOMIX beamline at Synchrotron SOLEIL (Gif-sur-Yvette, France) (Weitkamp et al., 2017). Here, an undulator gap of 10.3 mm was selected together with a  $20 \mu\text{m}$  Au filter to provide X-rays with an effective mean photon energy of around 22 keV. Radiographic projections were acquired with a detector system consisting of a  $300 \mu\text{m}$ -thick LuAG scintillator coupled to a scientific CMOS camera (Hamamatsu Orca Flash 4.0 V2,  $2048 \times 2048$  pixels,  $6.5 \mu\text{m}$  physical pixel size) via a lens system made of two photo objectives in tandem geometry (Hasselblad HC 4/210 and HC 2.2/100, numerical aperture of 0.22) resulting in a magnification factor of 2.1 and thus yielding an effective pixel size of  $3.1 \mu\text{m}$  (Desjardins et al., 2018). The detector system's resolution is the result of three factors: (i) Nyquist-Shannon sampling theorem, (ii) the Hasselblad objective quality (including mirror, etc.), and (iii) the "blur" within the scintillator. At 22 keV, most X-ray photons are absorbed in the first third of the scintillator: 87.9% (98.5%) of photons are absorbed by a depth of

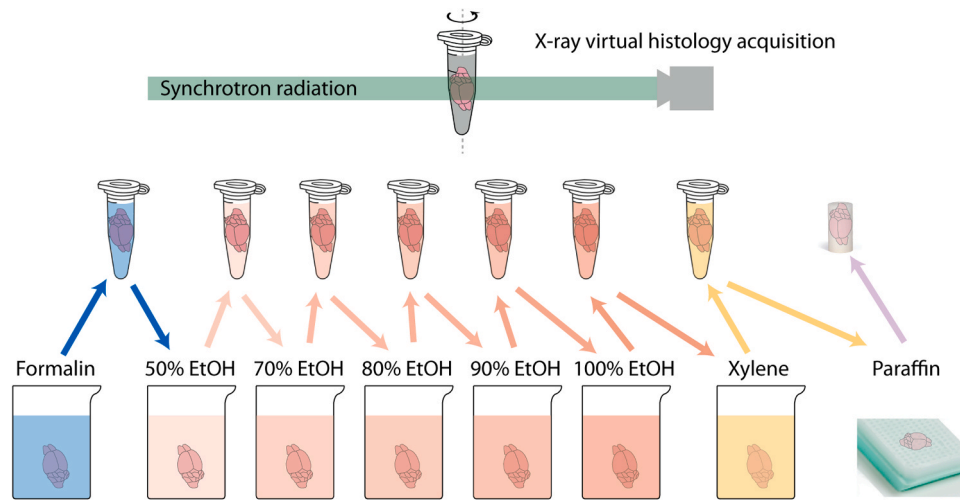


**Fig. 1.** Virtual histology of an entire mouse brain from formalin fixation to paraffin embedding. Between each step of the standard paraffin embedding protocol, the mouse brain was placed in an Eppendorf tube filled with the embedding media and measured at the ANATOMIX beamline (Synchrotron SOLEIL, Gif-sur-Yvette, France) with pixel length of 3.1  $\mu\text{m}$ . The final paraffin block was trimmed to a cylinder for measurement.

108  $\mu\text{m}$  (216  $\mu\text{m}$ ), corresponding to a maximal full width at half maximum blur of 1 pixel (2 pixels). Most well-designed detector systems offer spatial resolution of 2.5–3 pixels. Here, projections of a Siemens star test pattern showed that the setup could resolve a line pair with period just below 10  $\mu\text{m}$ .

The sample was placed 675 mm upstream of the detector to allow for edge enhancement. For tomographic acquisition, 5,900 projections were acquired over an angular range of 360° with off-axis alignment to nearly double the detector field-of-view. The exposure time was 50 ms per projection. The fly-scan mode was used to minimize overhead. The scan time for a single height step was around seven minutes. Three to four height steps were needed to capture the full sample depending on embedding state. The resulting datasets contained approximately 4,000  $\times$  4,000  $\times$  7,000 voxels and covered a volume of approximately 12  $\times$  12  $\times$  21 mm<sup>3</sup>.

The selected propagation distance caused edge enhancement, which was desired for the visualization of anatomical structures and interfaces between tissues of similar density. The experimental setup would have allowed for single-distance phase retrieval due to the propagation distance of 675 mm and spatial coherence at the ANATOMIX beamline of Synchrotron SOLEIL. Here, we opted for reconstruction of the linear attenuation coefficient  $\mu$ , herein referred to as the absorption coefficient, because it does not require *a priori* knowledge of sample composition and filtering for noise reduction can be applied without shifting mean  $\mu$ -values (Rodgers et al., 2020). Surprisingly, this approach provided sufficient contrast even in the formalin-fixed state despite the low absorption contrast (Schulz et al., 2010). The  $\mu$ -values measured at interfaces are not considered quantitative since phase effects were present.

For the photon energies and sample size used in this study, the photoelectric effect is the main contributor to X-ray absorption and thus  $\mu$  is related to the mass density  $\rho$  through  $\mu \propto \rho Z^4/E^3$ , with atomic number  $Z$  and photon energy  $E$  (Als-Nielsen and McMorrow, 2011). The reconstructed  $\mu$ -values are thus an approximate measure of mass density  $\rho$ , though the impact of phase-contrast phenomena and the energy spectrum used prevent accurate quantitative determination of  $\mu$ - or  $\rho$ -values.

### 2.3. Dose estimation and potential temperature increase of the mouse brain

The substantial radiation dose during microtomography at synchrotron radiation facilities should not be ignored. Nevertheless, no indication of radiation-induced changes was observed in this study:

projections at same orientation, *i.e.* rotation stage at 0° and 360°, as well as from adjacent height steps showed no noticeable changes in the overlap regions; bubble formation or sample discoloration were not observed; motion artifacts were not present in reconstructions.

The dose was approximated from an estimate of the total flux of the 22 keV-photons per detector pixel. We detected 40,000 and 20,000 counts per pixel without and with the sample, respectively. Considering the acquisition of 5,900 projections with the asymmetric rotation axis, the optical magnification of the detection unit and the scintillator efficiency, the total number of photons per pixel was about 10<sup>8</sup>, the deposited energy was 3 J and the dose was 3 kGy.

The absorbed energy of 3 J in the 1.5 g contents of the Eppendorf container, *i.e.* brain tissue and liquid with a heat capacity of around 4,000 J kg<sup>-1</sup> K<sup>-1</sup>, would lead to a maximal temperature increase of 0.5 K. This temperature increase gives rise to a linear thermal expansion of one tenth of the pixel length, which is in agreement with the lack of observations mentioned above.

### 2.4. Tomographic reconstruction

The reconstruction pipeline was implemented in Matlab (release R2020a, The MathWorks, Inc., Natick, USA). Prior to flat- and dark-field correction, radiographic projections were stitched together based on maximum cross-correlation. Ring correction was performed by taking a mean of all projections, applying a low-pass filter to isolate rings, and subtracting the result from the flat-field-corrected projections (a 2D variation of the 1D approach given in *e.g.* (Boin and Haibel, 2006; Miron et al., 2014)). A filtered back-projection with the standard Ram-Lak filter was used for tomographic reconstruction.

Filtering or binning were applied after ring correction to avoid increasing artifact strength (Vo et al., 2018). For the unbinned dataset, Gaussian filtering was used to improve contrast-to-noise at the expense of some spatial resolution (Rodgers et al., 2020). A Gaussian filter with  $\sigma = 1.25$  pixels was applied after reconstruction and prior to registration. Additionally, 3  $\times$  3 and 9  $\times$  9 binned projections, Gaussian filtered with  $\sigma = 1.5$  pixels prior to downsampling, were reconstructed to improve contrast-to-noise and reduce data size (Thurner et al., 2004) for memory-intensive computational steps such as non-rigid registration. The 3  $\times$  3  $\times$  3 binned tomographic data with voxel length of 9.3  $\mu\text{m}$  have been made publicly available (Rodgers et al., 2021).

## 2.5. Laboratory-based microtomography

To verify that contrast changes in the brain were observable in pure absorption contrast, an additional mouse brain was measured using a SkyScan 1275 (Bruker, Kontich, Belgium) laboratory microtomography scanner.

The tissue used was excess from an experiment approved by the veterinary office of the Canton of Zurich (license number ZH117/19). One 42 days-old female mouse was euthanized with carbon dioxide then the brain was excised and washed in phosphate buffered saline. The brain was then immersion-fixed in 10% neutral buffered formalin. The mouse line employed was derived from a crossing of three C57BL/6 reporter mouse lines encoding fluorescent proteins that do not impact endogenous gene expression (Yarg, Red5 and Smart13) (Molofsky et al., 2013; Reese et al., 2007; von Moltke, 2016). The mouse line is therefore equivalent to wild-type for the purposes of the current study. The fixation and embedding was performed in the same way as described in Section 2.1.

Laboratory microtomography measurements were taken in formalin, 100% ethanol, xylene, and paraffin. The same parameters were used for all four scans: the acceleration voltage was 25 kVp, electron beam current was 193  $\mu$ A, pixel size was 7.5  $\mu$ m, exposure time was 305 ms, the mean number of counts per pixel was 58,000 in the reference image, and 720 projections were taken around 360°. Beam hardening correction, ring artifact removal, and tomographic reconstruction were performed with the SkyScan NRecon software package (Version 1.7.4, Bruker, Kontich, Belgium).

## 2.6. Three-dimensional rendering and segmentation

Segmentation was performed with VGStudio MAX 2.1 (Volume Graphics, Heidelberg, Germany). Adaptive region-growing from user-defined seed points and subsequent morphological operations were used for semi-automatic segmentation of anatomical features. Segmentations were carried out by a single observer based on the Allen Mouse

Brain Atlas (Lein et al., 2007). To understand how over- and under-segmentation impacted the volume of the segmented structures, we morphologically dilated or eroded the single-observer segmentations with spheres of radius 3 voxels for the full brain and radius 1 voxel for the hippocampus, anterior commissure, and ventricles. These radii for dilation or erosion were chosen by the observer as the largest values that still resulted in an acceptable segmentation. The volumes of these dilated/eroded segmentations were used as error bars in Fig. 2 (right). The volume renderings of the segmentations found in Fig. 2 (left) were also generated with VGStudio MAX 2.1 (Volume Graphics, Heidelberg, Germany).

## 2.7. Quality assurance for data processing pipeline

We identified the following sources of artifacts or losses of data quality during the processing pipeline. Reconstruction (Section 2.4): ring, streak, center-of-rotation, and stitching/blending artifacts. Filtering (Section 2.4): noise, increasing ring artifacts, and over-smoothing. To avoid creating these artifacts, orthogonal slices of all datasets were visually inspected after each processing step. For consistency, parameters were selected only if they allowed for acceptable performance on all datasets.

## 3. Results

### 3.1. Global brain shrinkage

The datasets from each of the primary embedding steps (formalin, 100% ethanol, xylene, and paraffin) were manually segmented to track the volume of the full brain, hippocampus, anterior commissure olfactory and temporal limbs (hereafter “anterior commissure”), as well as the lateral and third ventricles (hereafter “ventricles”). The segmentations were based on the Allen Mouse Brain Atlas (Lein et al., 2007). Fig. 2 shows renderings of the segmented regions (left) and measured volumes (right). The measurements were taken from a single brain with

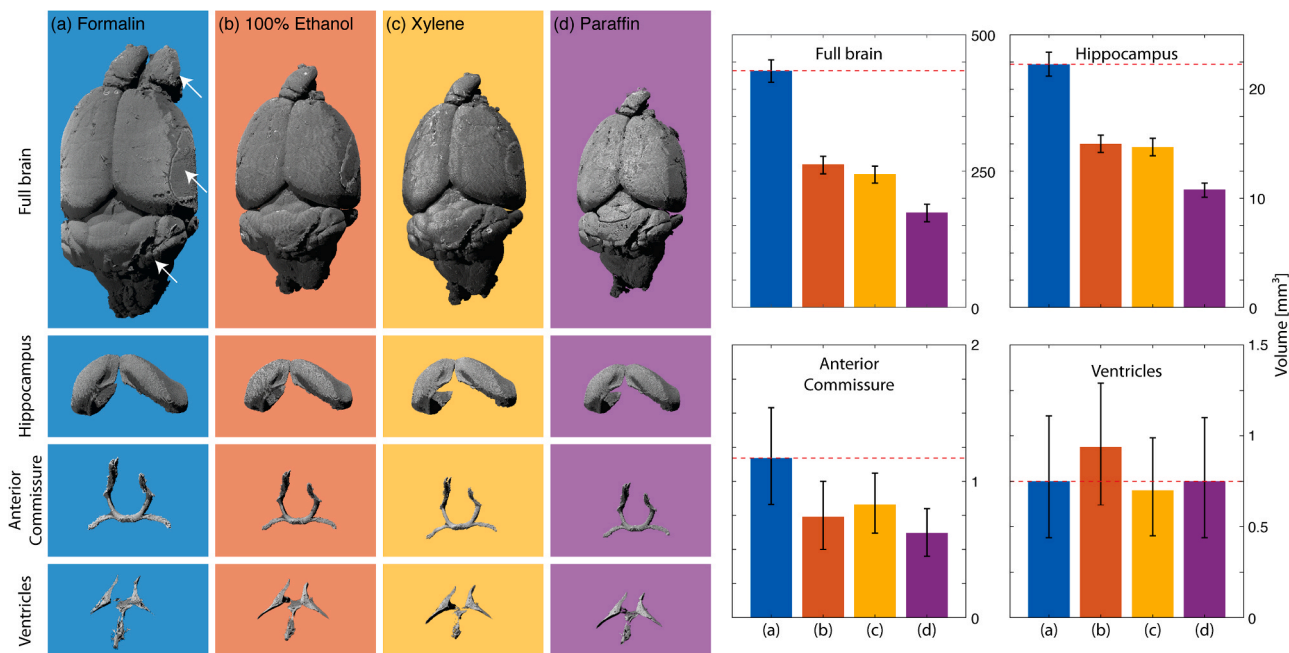


**Fig. 2.** Brain shrinkage over the course of paraffin embedding. (left) Volume renderings of manually segmented tomographic data are shown for the mouse brain and three selected anatomical regions after (a) formalin fixation, (b) dehydration in ascending alcohol solutions, (c) xylene, and (d) paraffin embedding. Arrows indicate (top) the olfactory lobe, which was broken during sample handling, (middle) the contact between container and brain, and (bottom) a cut on the cerebellum from the extraction of the brain. For reference, the width of the formalin-fixed brain at the middle arrow is about 8.5 mm and all of the renderings have the camera and sample in the same positions. (right) The bar charts show the volumes and estimates of inter-observer segmentation variability as error bars for the selected regions for each embedding step.

error bars representing simulated inter-observer variability. The volumes of the four segmented features and the related volume changes are given in Table 1. The volumes and volume changes are based on segmentations, which are displayed with volume renderings in Fig. 2. The volume changes given in Fig. 2 and Table 1 demonstrate that tissue shrinkage is non-uniform and varies across the selected anatomical features.

### 3.2. Density changes

In addition to the volume change, a reduction in the X-ray absorption coefficient  $\mu$  values of the brain tissue and surrounding medium was observed. Histograms of  $\mu$  for the volumetric datasets of the brain in formalin, 100% ethanol, xylene, and paraffin are displayed in Fig. 3 (left). The shift of the main peak towards lower  $\mu$  indicates decreased X-ray absorption within the tissue. A broadening of the histogram peak widths indicates an increase in inter-tissue density differences. These changes are also illustrated by axial slices through the datasets with the same grayscale range in Fig. 3 (right). The increase in inter-tissue density differences results in easier differentiation of anatomical features. Despite the mask to isolate the brain tissue, some of the embedding media is reflected in the histogram: formalin solution is more dense than the formalin-fixed brain (right shoulder in histogram) while for the other steps the embedding media are less dense than the brain (smaller peaks on the left side of the histograms).

Table 2 shows the measured absorption coefficients for regions of the cerebellum in formalin, 100% ethanol, xylene, and paraffin. The granular layer, molecular layer, and white matter were manually segmented and the mean values were measured. The absorption coefficient of formalin exceeded those of the other embedding materials. All features of the cerebellum had negative contrast to formalin and positive contrast to 100% ethanol, xylene, and paraffin. Contrast between the three segmented regions of the cerebellum and the surrounding medium increased from formalin to ethanol, xylene, and paraffin. The  $\mu$  difference between molecular layer and the granular layer increased over the embedding process. Contrast of white matter to granular layer was moderate in formalin and 100% ethanol, and increased in xylene and paraffin. Compared to white matter and the granular layer, the

**Table 1**

Volumes of the full brain, hippocampus, anterior commissure, and ventricles in the four primary embedding media. Volumes and volume ratio (percentage of volume in formalin) are based on the manual segmentations shown in Fig. 2. The given ranges indicate simulated inter-observer variability. We assume that observers will consistently over- or under-segment the datasets across all embeddings. Therefore, the ranges of volume change correspond to all over- or under-segmented volumes.

	Formalin	100% Ethanol	Xylene	Paraffin
Full brain				
Volume [mm <sup>3</sup> ]	434 413–454	262 245–277	244 228–259	174 157–189
Volume Ratio	–	60% 59–61%	56% 55–57%	40% 38–42%
Hippocampus				
Volume [mm <sup>3</sup> ]	22.3 21.2–23.4	15.0 14.2–15.8	14.7 13.9–15.5	10.8 10.1–11.4
Volume Ratio	–	67% 67–67%	66% 66–66%	48% 48–49%
Anterior Commissure				
Volume [mm <sup>3</sup> ]	1.17 0.83–1.54	0.74 0.50–1.00	0.83 0.62–1.06	0.62 0.45–0.80
Volume Ratio	–	63% 60–65%	71% 75–69%	53% 54–52%
Ventricles				
Volume [mm <sup>3</sup> ]	0.75 0.44–1.11	0.94 0.62–1.29	0.70 0.45–0.99	0.75 0.44–1.10
Volume Ratio	–	125% 141–116%	94% 102–89%	100% 100–99%

absorption coefficient of molecular layer was intermediate for formalin, smaller for ethanol, and intermediate for xylene and paraffin.

Table 3 shows the standard deviation  $\sigma$  of the absorption coefficient within the same regions as Table 2. This gives a measure of texture, or the difference in absorption between extracellular space and microscopic features such as cells, fibers, and vessels. Improved contrast of fine structures was demonstrated by increased  $\sigma$  values from formalin to subsequent steps. For example, the  $\sigma$  for white matter was highest in 100% ethanol. This observation agreed with visual assessment, where the texture of the fiber structures within the white matter was more discernible in 100% ethanol than for the other embedding stages (cf. Fig. 4 bottom). The increased  $\sigma$  of the paraffin was due its granular structure.

### 3.3. Laboratory- and synchrotron radiation-based microtomography

To confirm that the observed changes in X-ray absorption coefficient were not a result of phase effects, an additional mouse brain was measured in pure absorption mode with a laboratory microtomography system. Fig. 4 (top) shows virtual coronal slices through the cerebellum and brainstem from both laboratory and synchrotron radiation-based microtomography datasets. Magnified views (bottom) highlight the granular layer, molecular layer, white matter, and interposed nucleus of the cerebellum. Both modalities show the same contrast changes over the course of embedding, namely an increasing contrast between brain and surrounding medium, improved contrast between granular and molecular layers over the course of embedding, lower absorption of white matter relative to surrounding tissue in formalin, and increased absorption of white matter in 100% ethanol.

It should be noted that the higher resolution synchrotron radiation-based measurements allowed for differentiation of individual cells, vessels, and fiber tracts. The edge enhancement that is present in the synchrotron radiation datasets improves visualization of these structures. For example, the interposed nucleus of the cerebellum and the Purkinje cell layer (Fig. 4 bottom) can be distinguished in the datasets from ANATOMIX, but appear uniform in the laboratory-based datasets. While both datasets appear to have similar contrast, the synchrotron radiation-based datasets would have significantly higher contrast-to-noise ratio if they were blurred or binned to match the spatial resolution of the laboratory instrument (Rodgers et al., 2020; Thurner et al., 2004).

## 4. Discussion

Standard histological preparations include the exchange of formalin with alcohol, alcohol with xylene, and xylene with paraffin, a procedure that alters the densities of the affected soft tissues and thereby changes the local X-ray absorption values. Neurons, for example, show significant X-ray contrast enhancement from paraffin embedding, see e.g. (Töpperwien et al., 2019; Khimchenko et al., 2018). In this sense, sample embedding is analogous to staining and should be considered as an experimental parameter to be optimized. The understanding of tissue density and related X-ray contrast changes for the entire brain of animals and humans is therefore desirable, as it will facilitate the selection of embedding state for the visualization of the anatomical structure of interest. In this framework, we combined isotropic micrometer-resolution imaging in three dimensions (Part 1, this paper) with non-rigid registration (Part 2, (Rodgers et al., 2021a)) to quantify morphological and density changes as a result of tissue embedding steps. By way of example, we employed synchrotron radiation-based hard X-ray microtomography to map an entire mouse brain over the course of paraffin embedding, i.e. in formalin, five ascending ethanol solutions, xylene, and finally paraffin. The proposed procedure can be equally employed to any other kind of physically soft tissue with the aim to measure global and local volume changes, to identify the most appropriate embedding medium for feature visualization, and to reveal the basis for the

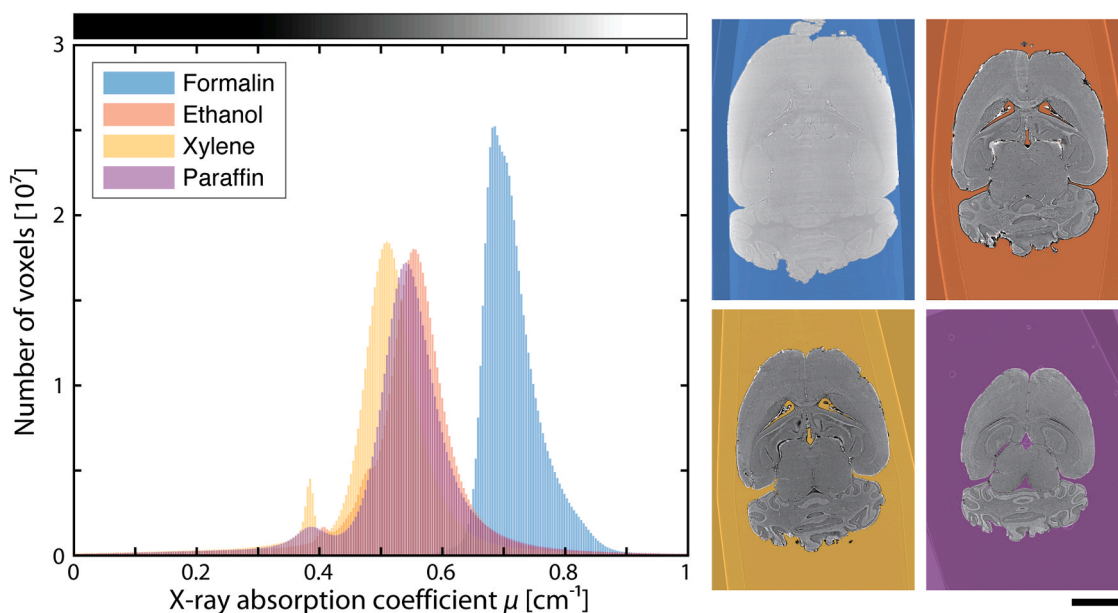


**Fig. 3.** Global density changes during embedding. Histograms of the X-ray absorption coefficient  $\mu$  within the brain for several stages of the paraffin embedding protocol. Related axial slices through the original (not registered) datasets are shown with the same grayscale range of  $\mu \in [0.3, 0.9] \text{ cm}^{-1}$  as indicated on the histograms. The scale bar for all images is 3 mm. The measurements were taken with the same acquisition parameters. The decrease in mean  $\mu$  indicates reduced tissue density and the broadening of the peaks indicates increasing separation of tissue densities. The embedding material (semitransparent color overlay on image), which is not completely masked out, accounts for the right shoulder in formalin histogram and the smaller left histogram peaks in the other media.

**Table 2**

X-ray contrast change in the cerebellum. For the formalin, 100% ethanol, xylene, and paraffin datasets, the mean absorption coefficient  $\mu$  was measured in manually segmented regions in the granular layer, molecular layer, and white matter of the cerebellum. Contrast between granular layer and both white matter and molecular layer increased with subsequent embedding steps. Molecular layer to white matter contrast was small in 100% ethanol, though texture of white matter increased (see Table 3).

	Mean absorption coefficient $\mu \text{ [cm}^{-1}\text{]}$			
	Embedding material	Molecular layer	Granular layer	White matter
Formalin	0.86	0.83	0.81	0.77
100% Ethanol	0.56	0.71	0.64	0.65
Xylene	0.45	0.69	0.59	0.58
Paraffin	0.45	0.78	0.66	0.62

**Table 3**

Increasing texture across the embedding process. The standard deviation  $\sigma$  of the absorption coefficient of structures in manually segmented regions of the cerebellum were measured for the formalin, 100% ethanol, xylene, and paraffin datasets. The  $\sigma$  within the selected regions rose as a result of increased density differences between the extracellular space and cells, fibers, vessels, etc. The  $\sigma$  of the embedding material indicates the noise level, except in paraffin, which had a inhomogeneous granular structure.

	Standard deviation $\sigma \text{ [cm}^{-1}\text{]}$			
	Embedding material	Molecular layer	Granular layer	White matter
Formalin	0.05	0.07	0.06	0.07
100% Ethanol	0.05	0.21	0.16	0.20
Xylene	0.05	0.24	0.16	0.16
Paraffin	0.13	0.24	0.19	0.16

dramatic X-ray contrast enhancement observed in numerous embedded tissues.

We have demonstrated X-ray virtual histology for slicing-free imaging of an entire mouse brain after each of the primary steps of tissue preparation for conventional histology, namely fixed in formalin, immersed in ethanol solutions (50%, 70%, 80%, 90%, and 100%), immersed in xylene, and embedded in a paraffin block. These volumetric datasets with voxel length of  $3.1 \mu\text{m}$  allowed for analysis of morphological changes and X-ray contrast enhancement. The present study is based on a single mouse brain, thus it is of a preliminary nature compared to MRI-based brain atlases that include six to 20 mice per sex (Dorr et al., 2008). A sample size of a few tens of mice is feasible for future experiments based on the 30 min per brain acquisition time of the synchrotron radiation-based imaging presented here.

X-ray virtual histology provides full brain imaging with near micrometer resolution and reasonable contrast from formalin fixation to paraffin embedding. For *in vivo* studies, however, the radiation dose limitations and the strongly X-ray absorbing skull prevent such high-resolution brain imaging. Therefore, the present study treats the formalin-fixed state as the reference. Fresh tissue imaging would also be possible within a 30-minute scan time, potentially providing a reference point closer to the *in vivo* state. This would, however, present logistical complications related to safety, animal housing, surgery, and timing of experiments. Alternatively, MRI allows for *in vivo* and *post mortem* measurements (Ma et al., 2008), but only reaches a spatial resolution of around 100 micrometers. A combination of the imaging techniques could allow for detailed studies of the changes from the *in vivo* state via formalin fixation to the paraffin embedded state.

We analyzed brain shrinkage during the embedding protocol with two methods: manual segmentation of anatomical features (Part 1) and non-rigid registration (Part 2). The segmentation-based approach allowed for calculation of the volume of the full brain and anatomical regions such as the ventricles, anterior commissure, and the hippocampus (Fig. 2). The improved spatial resolution of microtomography compared to MR microscopy should lead to more accurate segmentations and volume measurements. Multiple independent observers would be needed to fully confirm this hypothesis, whereas the present study

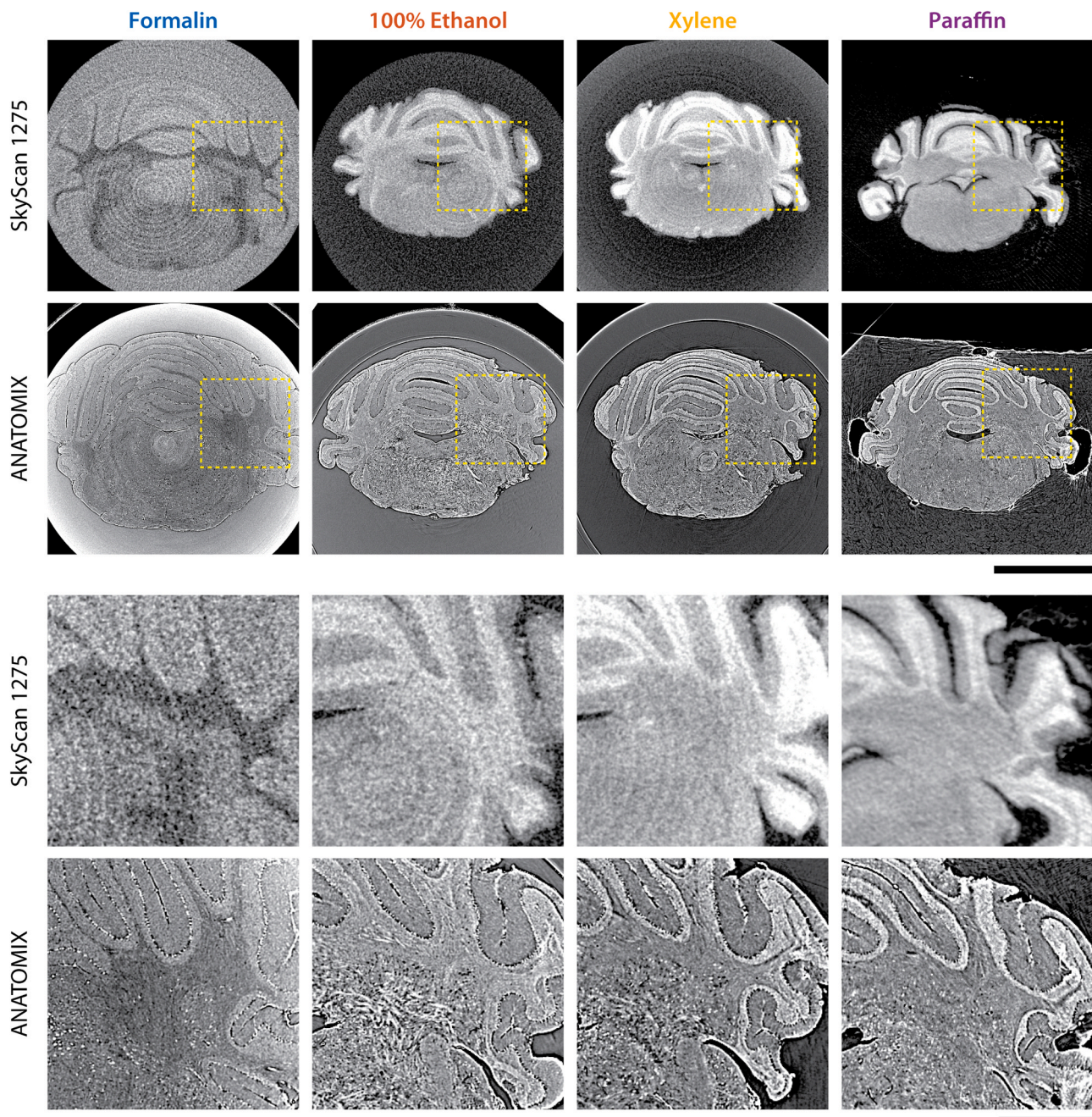


**Fig. 4.** Comparing tissue contrast in laboratory- and synchrotron radiation-based microtomography of two mouse brains across the embedding media. Similar coronal slices are shown through a mouse brain measured in absorption-contrast mode in a SkyScan 1275 (Bruker, Kontich, Belgium) system and the mouse brain measured at ANATOMIX beamline, Synchrotron SOLEIL (Gif-sur-Yvette, France). These slices contain (top) the cerebellum and the brain stem, while magnified views (bottom) focus on the granular layer, molecular layer, and white matter of the cerebellum, as well as the interposed nucleus. Despite the presence of edge enhancement, the contrast changes observed at ANATOMIX based on reconstructed absorption values are also observed in the laboratory with pure absorption contrast.

was based on a single-observer study and relied on morphological operations to simulate inter-observer variability. Still, the segmentation-based approach was sufficient to determine that volume change was inhomogeneous. Unfortunately, a full characterization of shrinkage with this approach would require extensive segmentation.

Automated segmentation of label-free X-ray microtomography data with cellular resolution is challenging because anatomical borders are often based on connectivity or function and are thus not directly correlated to density. Manual or semi-automatic approaches are required, though ambiguities in anatomical borders cause these approaches to be slow and to suffer from user-specific variability. The

registration approach presented in Part 2 and in (Rodgers et al., 2021b) involves relatively few user interactions. An additional registration between the reference dataset and an appropriate atlas would allow for propagation of all the atlas labels with similar accuracy to the manual approach. This atlas-based segmentation will be more efficient as the number of anatomical features and/or number of datasets increases.

The formalin-fixed brain was squeezed into the Eppendorf container, see Fig. 2. The contact with the container affected tissue up to about 0.5 mm from the edge, see Part 2 Fig. 3.

We acquired a total of nine quasistatic measurements, each after 2 h of immersion in the embedding media, which is a standard immersion

time found in paraffin embedding protocols. Time-resolved volumetric imaging will give a deeper insight into the feature-dependent formation of local strains through the diffusion of the embedding media and its reactions with the tissue components. The current acquisition time was around 30 min, whereas time resolution of around 1 min would be desirable for real-time tracking of shrinkage. Reducing the size of the sample (e.g. a study of tissue punches), the spatial resolution, and/or the signal-to-noise ratio will be necessary to achieve this with currently available instrumentation.

In addition to shrinkage, we analyzed the X-ray absorption changes at each step of the embedding protocol. While the setup allowed for phase retrieval, we analyzed  $\mu$  because it does not require *a priori* knowledge of sample composition and noise reduction filtering can be applied without shifting mean  $\mu$ -values (Rodgers et al., 2020). Despite the semi-quantitative nature of the measurement, we can infer composition changes from mean  $\mu$  of large anatomical regions and texture changes from the standard deviation of  $\mu$ . To confirm the findings reported here based on a mixture of phase- and absorption-contrast, we performed pure absorption-contrast measurements of a second brain with a laboratory instrument. The results confirmed the observed contrast changes, see Fig. 4.

In preparation steps subsequent to formalin, a decrease in X-ray absorption of both brain tissue and surrounding solutions was observed (Fig. 3). The average absorption decreases of the embedding media compared to formalin are due to a decrease in both density and effective atomic number: formalin (approximated by water, H<sub>2</sub>O) has density 0.997 g mL<sup>-1</sup>, ethanol (C<sub>2</sub>H<sub>6</sub>O) has density 0.789 g mL<sup>-1</sup>, xylene (C<sub>8</sub>H<sub>10</sub>) has density 0.864 g mL<sup>-1</sup>, and paraffin (C<sub>n</sub>H<sub>2n+2</sub>) has density around 0.900 g mL<sup>-1</sup>. The mean absorption of the brain was not proportional to the embedding medium: the formalin-fixed brain was less than that of formalin, while the brain was higher absorbing than the surrounding medium in ethanol, xylene, and paraffin.

The reduction in mean absorption from formalin to ethanol, xylene, and paraffin is accompanied by an increase in absorption differences between internal structures, evidenced by broadening of histogram peaks in Fig. 3 as well as larger  $\sigma$  values in Table 3. Generally, these changes result in an improved visualization of internal structures with X-ray microtomography for subsequent embedding steps.

Interestingly, the relative absorption values of tissues change substantially from one embedding step to the next: subsequent steps show enhanced or in some cases inverted contrast between internal structures (Table 2). This indicates an embedding medium can be selected to best highlight a given anatomical feature, analogous to stain selection.

Our results indicate that ethanol immersion or paraffin embedding should generally be favored for microtomography-based virtual histology. Compared to formalin, both of these preparations provide X-ray contrast gains within the brain and from the brain to the surrounding medium. These properties also simplify alignment and navigation during imaging. The global decrease in absorption allows for the selection of a lower photon energy to improve density resolution. Töpperwien and co-workers have also noted that compared to formalin, both ethanol and paraffin embedding provide improved contrast for imaging individual cells (Töpperwien et al., 2019). From a practical standpoint, the paraffin embedded state is the simplest to handle and measure. Formalin and xylene both pose health risks and the selection of organic solvent resistant container is an additional requirement for xylene. Future studies should consider the radiation resistance of the embedding media presented here, particularly under higher doses necessary for X-ray nanotomography of brain tissue (Khimchenko et al., 2018; Kuan et al., 2020) as it is scaled towards macroscopic specimens (Du et al., 2021).

All of the specimen preparation steps studied here are compatible with prior *in vivo* MRI or subsequent conventional histology. In principle, non-rigid registration of high resolution virtual histology data to *in vivo* MRI (Fratini et al., 2020) could allow for correction of deformations due to death, fixation, and subsequent tissue treatment. In this case, formalin offers the smallest deformations, though difficulty of

registration may be increased by lower image quality. Paraffin embedding offers the smallest deformations in the case of slice-to-volume registration of conventional histology to virtual histology (Chicherova et al., 2018; Ferrante and Paragios, 2017).

We have presented staining- and slicing-free X-ray imaging of a full mouse brain with pixel size of 3.1  $\mu$ m. For full-field tomographic imaging, the accessible spatial resolution depends on the object size. Additional stitching of data will allow for the measurement of the full mouse brain with a spatial resolution of about one micrometer. X-ray imaging with pixel sizes at or below 1  $\mu$ m has been reported in literature, however detailed images of those datasets are not yet publicly accessible (Vescovi, 2018; Miettinen et al., 2019). Based on the present study, a decrease in pixel size to below 1  $\mu$ m appears feasible, though the approximately 10-fold increase in measurement time and data size are challenges. Increasing spatial resolution with fixed image quality will dramatically increase dose, therefore radiation damage may be observed for such measurements. The current results and extensions to higher resolution suggest that microtomography data should be integrated into future mouse brain atlases.

## 5. Conclusions

We employed slicing-free, three-dimensional virtual histology of a mouse brain to quantify morphology and X-ray contrast changes during the standard protocol for tissue preparation from the formalin-fixed state to the paraffin-embedded state. The mouse brain volume was 60%, 56%, and 40% of that in formalin for 100% ethanol, xylene, and paraffin, respectively. The volume changes of anatomical regions such as the hippocampus, anterior commissure, and ventricles were not proportional to the global volume change. Additionally, subsequent steps of the embedding protocol led to a global decrease in X-ray absorption as well as changes in inter-tissue absorption. These X-ray absorption changes make ethanol immersion or paraffin embedding attractive choices for X-ray microtomography. These virtual histology results can complement mouse brain atlases based on a combination of magnetic resonance microscopy and optical micrographs of serial histological sections.

## CRedit author contribution statement

**Griffin Rodgers:** Conceptualization, Methodology, Software, Formal analysis, Investigation, Data curation, Writing – original draft, Writing – review & editing, Visualization, Funding acquisition. **Willy Kuo:** Methodology, Validation, Investigation, Resources, Writing – review & editing. **Georg Schulz:** Conceptualization, Methodology, Investigation, Writing – review & editing, Visualization, Supervision. **Mario Scheel:** Formal analysis, Investigation, Resources, Writing – review & editing. **Alexandra Migga:** Validation, Formal analysis, Writing – review & editing, Visualization. **Christos Bikis:** Formal analysis, Writing – review & editing. **Christine Tanner:** Writing – review & editing, Visualization, Supervision. **Vartan Kurtcuoglu:** Writing – review & editing, Supervision, Project administration, Funding acquisition. **Timm Weitkamp:** Investigation, Resources, Writing – review & editing, Funding acquisition. **Bert Müller:** Conceptualization, Methodology, Investigation, Resources, Writing – review & editing, Visualization, Supervision, Project administration, Funding acquisition.

## Data availability

The tomographic data from all preparation steps are publicly available in a Zenodo repository (<https://doi.org/10.5281/zenodo.4651412>) (Rodgers et al., 2021). The 3 $\times$  downsampled volumes can be immediately downloaded. Due to the large data sizes, the full resolution data will be made available by request to the first author.

## Acknowledgment

This work was carried out under Synchrotron SOLEIL experiment No. 20190424. The authors thank J. Perrin and D. Guillaume of the ANATOMIX beamline at Synchrotron SOLEIL for support during the beam time. ANATOMIX is an Equipment of Excellence (EQUIPEX) funded by the Investments for the Future program of the French National Research Agency (ANR), project NanoimagesX, grant no. ANR-11-EQPX-0031. The authors thank V. Meskenaitė and J. de Tenorio of the University of Zurich for providing excess cadavers for sample extraction. W. K. and V.K acknowledge support from the Swiss National Science Foundation via NCCR Kidney.CH and Project No. 153523. G.R., C.T., and B.M. acknowledge support from the Swiss National Science Foundation Project No. 185058.

## Declaration of Competing Interest

None.

## References

- Albers, J., Pacilé, S., Markus, M., Wiart, M., Vande Velde, G., Tromba, G., Dullin, C., 2018a. X-ray-based 3d virtual histology-adding the next dimension to histological analysis. *Mol. Imaging Biol.* 20 (5), 732–741. <https://doi.org/10.1007/s11307-018-1246-3>.
- Albers, J., Markus, M.A., Alves, F., Dullin, C., 2018b. X-ray based virtual histology allows guided sectioning of heavy ion stained murine lungs for histological analysis. *Sci. Rep.* 8 (1), 7712. <https://doi.org/10.1038/s41598-018-26086-0>.
- Als-Nielsen, J., McMorrow, D., 2011. *Elements of Modern X-ray Physics*, second ed. John Wiley & Sons, New York. <https://doi.org/10.1002/9781119998365>.
- Amunts, K., Lepage, C., Borgeat, L., Mohlberg, H., Dickscheid, T., Rousseau, M.-É., Bludau, S., Bazin, P.-L., Lewis, L.B., Oros-Peusquens, A.-M., Shah, N.J., Lippert, T., Zilles, K., Evans, A.C., 2013. Bigbrain: an ultrahigh-resolution 3D human brain model. *Science* 340 (6139), 1472–1475. <https://doi.org/10.1126/science.1235381>.
- Anderson, R., Maga, A.M., 2015. A novel procedure for rapid imaging of adult mouse brains with microCT using iodine-based contrast. *PLoS One* 10 (11), e0142974. <https://doi.org/10.1371/journal.pone.0142974>.
- Barbone, G.E., Bravin, A., Romanelli, P., Mittone, A., Bucci, D., Gaaß, T., Le Duc, G., Auweter, S., Reiser, M.F., Kraiger, M.J., Hrabě de Angelis, M., Battaglia, G., Coan, P., 2018. Micro-imaging of brain cancer radiation therapy using phase-contrast computed tomography. *Int. J. Radiat. Oncol. Biol. Phys.* 101 (4), 965–984. <https://doi.org/10.1016/j.ijrobp.2018.03.063>.
- Barbone, G.E., Bravin, A., Mittone, A., Kraiger, M.J., Hrabě de Angelis, M., Bossi, M., Ballarini, E., Rodriguez-Mendez, V., Ceresa, C., Cavaletti, G., Coan, P., 2020. Establishing sample-preparation protocols for X-ray phase-contrast CT of rodent spinal cords: aldehyde fixations and osmium impregnation. *J. Neurosci. Methods* 339, 108744. <https://doi.org/10.1016/j.jneumeth.2020.108744>.
- Böhm, T., Joseph, K., Kirsch, M., Moroni, R., Hilger, A., Osenberg, M., Manke, I., Johnston, M., Stieglitz, T., Hofmann, U.G., Haas, C.A., Thiele, S., 2019. Quantitative synchrotron X-ray tomography of the material-tissue interface in rat cortex implanted with neural probes. *Sci. Rep.* 9 (1), 7646. <https://doi.org/10.1038/s41598-019-42544-9>.
- Boin, M., Haibel, A., 2006. Compensation of ring artefacts in synchrotron tomographic images. *Opt. Express* 14 (25), 12071–12075. <https://doi.org/10.1364/OE.14.012071>.
- Busse, M., Müller, M., Kimm, M.A., Ferstl, S., Allner, S., Achterhold, K., Herzen, J., Pfeiffer, F., 2018. Three-dimensional virtual histology enabled through cytoplasm-specific X-ray stain for microscopic and nanoscopic computed tomography. *Proc. Natl. Acad. Sci. USA* 115 (10), 2293–2298. <https://doi.org/10.1073/pnas.1720862115>.
- de Castro Fonseca, M., Araujo, B.H.S., Dias, C.S.B., Archilha, N.L., Neto, D.P.A., Cavalheiro, E., Westfahl, H., daSilva, A.J., Franchini, K.G., 2018. High-resolution synchrotron-based X-ray microtomography as a tool to unveil the three-dimensional neuronal architecture of the brain. *Sci. Rep.* 8 (1), 12074. <https://doi.org/10.1038/s41598-018-30501-x>.
- Chicherova, N., Hieber, S., Khimchenko, A., Bikis, C., Müller, B., Cattin, P., 2018. Automatic deformable registration of histological slides to  $\mu$ CT volume data. *J. Microsc.* 271 (1), 49–61. <https://doi.org/10.1111/jmi.12692>.
- Culling, C., 1974. *Methods of examination of tissues and cells*. In: Culling, C. (Ed.), *Handbook of Histopathological and Histochemical Techniques*, third ed. Butterworth-Heinemann, pp. 19–25. <https://doi.org/10.1016/B978-0-407-72901-8.50009-3>.
- D. Desjardins, A. Carcy, J. Giorgetta, C. Menneglier, M. Scheel, T. Weitkamp, Design of Indirect X-Ray Detectors for Tomography on the Anatomix Beamline, in: Proc. 10th Mechanical Engineering Design of Synchrotron Radiation Equipment and Instrumentation (MEDSIA18), Paris, France, 25–29 June 2018, no. 10 in Mechanical Engineering Design of Synchrotron Radiation Equipment and Instrumentation, JACoW Publishing, 2018, pp. 355–357. doi: 10.18429/JACoW-MEDSIA18-THPH09.
- Dorr, A., Lerch, J., Spring, S., Kabani, N., Henkelman, R., 2008. High resolution three-dimensional brain atlas using an average magnetic resonance image of 40 adult c57bl/6j mice. *NeuroImage* 42 (1), 60–69. <https://doi.org/10.1016/j.neuroimage.2008.03.037>.
- Du, M., Di, Z., Gürsoy, D., Xian, R.P., Kozorovitskiy, Y., Jacobsen, C., 2021. Upscaling X-ray nanoimaging to macroscopic specimens. *J. Appl. Cryst.* 54 (2), 386–401. <https://doi.org/10.1107/S1600576721000194>.
- Dyer, E.L., GrayRonal, W., Prasad, J.A., Fernandes, H.L., Gürsoy, D., De Andrade, V., Fezzaa, K., Xiao, X., Vogelstein, J.T., Jacobsen, C., Kording, K.P., Kasthuri, N., 2017. Quantifying mesoscale neuroanatomy using X-ray microtomography. *eNeuro* 4 (5). <https://doi.org/10.1523/ENEURO.0195-17.2017>.
- Ferrante, E., Paragios, N., 2017. Slice-to-volume medical image registration: a survey. *Med. Image Anal.* 39, 101–123. <https://doi.org/10.1016/j.media.2017.04.010>.
- Fratini, M., Abdollahzadeh, A., DiNuzzo, M., Salo, R.A., Maugeri, L., Cedola, A., Giove, F., Gröhn, O., Tohka, J., Sierra, A., 2020. Multiscale imaging approach for studying the central nervous system: methodology and perspective. *Front. Neurosci.* 14, 72. <https://doi.org/10.3389/fnins.2020.00072>.
- Germann, M., Morel, A., Beckmann, F., Andronache, A., Jeanmonod, D., Müller, B., 2008. Strain fields in histological slices of brain tissue determined by synchrotron radiation-based micro computed tomography. *J. Neurosci. Methods* 170 (1), 149–155. <https://doi.org/10.1016/j.jneumeth.2008.01.011>.
- Gong, H., Zeng, S., Yan, C., Lv, X., Yang, Z., Xu, T., Feng, Z., Ding, W., Qi, X., Li, A., Wu, J., Luo, Q., 2013. Continuously tracing brain-wide long-distance axonal projections in mice at a one-micron voxel resolution. *NeuroImage* 74, 87–98. <https://doi.org/10.1016/j.neuroimage.2013.02.005>.
- Hieber, S.E., Bikis, C., Khimchenko, A., Schweighauser, G., Hench, J., Chicherova, N., Schulz, G., Müller, B., 2016. Tomographic brain imaging with nuclear detail and automatic cell counting. *Sci. Rep.* 6, 32156. <https://doi.org/10.1038/srep32156>.
- Jiang, L., Li, C., Li, M., Yin, X., Wu, T., Duan, C., Cao, Y., Lu, H., Hu, J., 2021. Simultaneous 3D visualization of the microvascular and neural network in mouse spinal cord using synchrotron radiation micro-computed tomography. *Neurosci. Bull.* <https://doi.org/10.1007/s12264-021-00715-7>.
- Katsamenis, O.L., Olding, M., Warner, J.A., Chatelet, D.S., Jones, M.G., Sgalla, G., Smit, B., Larkin, O.J., Haig, I., Richeldi, L., Sinclair, I., Lackie, P.M., Schneider, P., 2019. X-ray micro-computed tomography for nondestructive three-dimensional (3D) X-ray histology. *Am. J. Pathol.* 189 (8), 1608–1620. <https://doi.org/10.1016/j.ajpath.2019.05.004>.
- Khimchenko, A., Deyhle, H., Schulz, G., Schweighauser, G., Hench, J., Chicherova, N., Bikis, C., Hieber, S.E., Müller, B., 2016. Extending two-dimensional histology into the third dimension through conventional micro computed tomography. *NeuroImage* 139, 26–36. <https://doi.org/10.1016/j.neuroimage.2016.06.005>.
- Khimchenko, A., Bikis, C., Pacureanu, A., Hieber, S.E., Thalmann, P., Deyhle, H., Schweighauser, G., Hench, J., Frank, S., Müller-Geberl, M., Schulz, G., Cloetens, P., Müller, B., 2018. Hard X-ray nanoholotomography: large-scale, label-free, 3D neuroimaging beyond optical limit. *Adv. Sci.* 5 (6), 1700694. <https://doi.org/10.1002/adv.201700694>.
- Kuan, A.T., Phelps, J.S., Thomas, L.A., Nguyen, T.M., Han, J., Chen, C.-L., Azevedo, A.W., Tuthill, J.C., Funke, J., Cloetens, P., Pacureanu, A., Lee, W.-C.A., 2020. Dense neuronal reconstruction through X-ray holographic nano-tomography. *Nat. Neurosci.* 23 (12), 1637–1643. <https://doi.org/10.1038/s41593-020-0704-9>.
- Lein, E.S., Hawrylycz, M.J., Ao, N., Ayres, M., Bensinger, A., Bernard, A., Boe, A.F., Boguski, M.S., Brockway, K.S., Byrnes, E.J., Chen, L., Chen, L., Chen, T.-M., ChiChin, M., Chong, J., Crook, B.E., Czaplinski, A., Dang, C.N., Datta, S., Dee, N.R., Desaki, A.L., Desta, T., Diep, E., Dolbeare, T.A., Donelan, M.J., Dong, H.-W., Dougherty, J.G., Duncan, B.J., Ebbert, A.J., Eichele, G., Estin, L.K., Faber, C., Facer, B.A., Fields, R., Fischer, S.R., Fliess, T.P., Frensley, C., Gates, S.N., Gattfelder, K.J., Halverson, K.R., Hart, M.R., Hohmann, J.G., Howell, M.P., Jeung, D.P., Johnson, R.A., Karr, P.T., Kawai, R., Kidney, J.M., Knapik, R.H., Kuan, C.L., Lake, J.H., Laramée, A.R., Larsen, K.D., Lau, C., Lemon, T.A., Liang, A.J., Liu, Y., Luong, L.T., Michaels, J., Morgan, J.J., Morgan, R.J., Mortrud, M.T., Mosqueda, N.F., Ng, L.L., Ng, R., Orta, G.J., Overly, C.C., Pak, T.H., Parry, S.E., Pathak, S.D., Pearson, O.C., Puchalski, R.B., Riley, Z.L., Rockett, H.R., Rowland, S.A., Royall, J.J., Ruiz, M.J., Sarno, N.R., Schaffnit, K., Shapovalova, N.V., Svisay, T., Slaughterbeck, C.R., Smith, S.C., Smith, K.A., Smith, B.I., Sotd, A.J., Stewart, N.N., Stumpf, K.-R., Sunkin, S.M., Sutram, M., Tam, A., Teemer, C.D., Thaller, C., Thompson, C.L., Varnam, L.R., Visel, A., Whitlock, R.M., Wohnoutka, P.E., Wolkey, C.K., Wong, V.Y., Wood, M., Yayaolu, M.B., Young, R.C., Youngstrom, B. L., Feng Yuan, X., Zhang, B., Zwingman, T.A., Jones, A.R., 2007. Genome-wide atlas 971 of gene expression in the adult mouse brain. *Nature* 445, 168–176. <https://doi.org/10.1038/nature05453>.
- Ma, Y., Smith, D., Hof, P., Foerster, B., Hamilton, S., Blackband, S., Yu, M., Benveniste, H., 2008. In vivo 3d digital atlas database of the adult c57bl/6j mouse brain by magnetic resonance microscopy. *Front. Neuroanat.* 2, 1. <https://doi.org/10.3389/neuro.05.001.2008>.
- Massimi, L., Bukreeva, I., Santamaria, G., Fratini, M., Corbelli, A., Brun, F., Fumagalli, S., Maugeri, L., Pacureanu, A., Cloetens, P., Pieroni, N., Fiordaliso, F., Forloni, G., Uccelli, A., Kerlero de Rosbo, N., Balducci, C., Cedola, A., 2019. Exploring Alzheimer's disease mouse brain through X-ray phase contrast tomography: from the cell to the organ. *NeuroImage* 184, 490–495. <https://doi.org/10.1016/j.neuroimage.2018.09.044>.
- Miettinen, A., Oikonomidis, I.V., Bonnin, A., Stampanoni, M., 2019. NRStitcher: non-rigid stitching of terapixel-scale volumetric images. *Bioinformatics* 35 (24), 5290–5297. <https://doi.org/10.1093/bioinformatics/btz423>.
- Mirone, A., Brun, E., Gouillart, E., Tafforeau, P., Kieffer, J., 2014. The PyHST2 hybrid distributed code for high speed tomographic reconstruction with iterative reconstruction and a priori knowledge capabilities. *Nucl. Instrum. Methods Phys.*

- Res., B 324, 41–48. <https://doi.org/10.1016/j.nimb.2013.09.030> (1st International Conference on Tomography of Materials and Structures).
- Mizutani, R., Suzuki, Y., 2012. X-ray microtomography in biology. *Micron* 43 (2), 104–115. <https://doi.org/10.1016/j.micron.2011.10.002>.
- Mizutani, R., Takeuchi, A., Uesugi, K., Ohyama, M., Takekoshi, S., Osamura, R.Y., Suzuki, Y., 2008. Three-dimensional microtomographic imaging of human brain cortex. *Brain Res.* 1199, 53–61. <https://doi.org/10.1016/j.brainres.2008.01.029>.
- Molofsky, A.B., Nussbaum, J.C., Liang, H.-E., Van Dyken, S.J., Cheng, L.E., Mohapatra, A., Chawla, A., Locksley, R.M., 2013. Innate lymphoid type 2 cells sustain visceral adipose tissue eosinophils and alternatively activated macrophages. *J. Exp. Med.* 210 (3), 535–549. <https://doi.org/10.1084/jem.20121964>.
- von Moltke, J., Ji, M., Liang, H.-E., Locksley, R.M., 2016. Tuft-cell-derived IL-25 regulates an intestinal ILC2–epithelial response circuit. *Nature* 529 (7585), 221–225. <https://doi.org/10.1038/nature16161>.
- Momose, A., 2005. Recent advances in X-ray phase imaging. *Jpn. J. Appl. Phys.* 44 (9A), 6355–6367. <https://doi.org/10.1143/jjap.44.6355>.
- Pichat, J., Iglesias, J.E., Yousry, T., Ourselin, S., Modat, M., 2018. A survey of methods for 3D histology reconstruction. *Med. Image Anal.* 46, 73–105. <https://doi.org/10.1016/j.media.2018.02.004>.
- Pinzer, B., Cacquevel, M., Modregger, P., McDonald, S., Bensadoun, J., Thuring, T., Aebischer, P., Stapanoni, M., 2012. Imaging brain amyloid deposition using grating-based differential phase contrast tomography. *NeuroImage* 61 (4), 1336–1346. <https://doi.org/10.1016/j.neuroimage.2012.03.029>.
- Questa, R., Schröder, R., 1997. The shrinkage of the human brain stem during formalin fixation and embedding in paraffin. *J. Neurosci. Methods* 75 (1), 81–89. [https://doi.org/10.1016/S0165-0270\(97\)00050-2](https://doi.org/10.1016/S0165-0270(97)00050-2).
- Reese, T.A., Liang, H.-E., Tager, A.M., Luster, A.D., Van Rooijen, N., Voehringer, D., Locksley, R.M., 2007. Chitin induces accumulation in tissue of innate immune cells associated with allergy. *Nature* 447 (7140), 92–96. <https://doi.org/10.1038/nature05746>.
- G. Rodgers, G. Schulz, W. Kuo, C. Tanner, B. Müller, Microtomography of a mouse brain from formalin fixed to paraffin embedded: datasets and registration parameters, 2021, March, doi: 10.5281/zenodo.4651412.
- Rodgers, G., Schulz, G., Deyhle, H., Kuo, W., Rau, C., Weitkamp, T., Müller, B., 2020. Optimizing contrast and spatial resolution in hard X-ray tomography of medically relevant tissues. *Appl. Phys. Lett.* 116 (2), 023702 <https://doi.org/10.1063/1.5133742>.
- Rodgers, G., Tanner, C., Schulz, G., Migga, A., Kuo, W., Bikis, C., Scheel, M., Kurtcuoglu, V., Weitkamp, T., Müller, B., 2021a. Virtual histology of an entire mouse brain from formalin fixation to paraffin embedding. Part 2: volumetric strain fields and local contrast changes. *J. Neurosci. Methods*.
- Rodgers, G., Schulz, G., Kuo, W., Scheel, M., Kurtcuoglu, V., Weitkamp, T., Müller, B., Tanner, C., 2021b. Non-rigid registration to determine strain fields during mouse brain fixation and embedding. *Proc. SPIE* 11586 (11586I), 55–65. <https://doi.org/10.1117/12.2583632>.
- Saccomano, M., Albers, J., Tromba, G., Dobrivojević Radmilović, M., Gajović, S., Alves, F., Dullin, C., 2018. Synchrotron inline phase contrast  $\mu$ CT enables detailed virtual histology of embedded soft-tissue samples with and without staining. *J. Synchrotron Radiat.* 25 (4), 1153–1161. <https://doi.org/10.1107/S1600577518005489>.
- Schulz, G., Weitkamp, T., Zanette, I., Pfeiffer, F., Beckmann, F., David, C., Rutishauser, S., Reznikova, E., Müller, B., 2010. High-resolution tomographic imaging of a human cerebellum: comparison of absorption and grating-based phase contrast. *J. R. Soc. Interface* 7 (53), 1665–1676. <https://doi.org/10.1098/rsif.2010.0281>.
- Thurner, P., Beckmann, F., Müller, B., 2004. An optimization procedure for spatial and density resolution in hard X-ray micro-computed tomography. *Nucl. Instrum. Methods Phys. Res. B* 225 (4), 599–603. <https://doi.org/10.1016/j.nimb.2004.05.027>.
- Töpperwien, M., van der Meer, F., Stadelmann, C., Salditt, T., 2018. Three-dimensional virtual histology of human cerebellum by X-ray phase-contrast tomography. *Proc. Natl. Acad. Sci. USA* 115 (27), 6940–6945. <https://doi.org/10.1073/pnas.1801678115>.
- Töpperwien, M., Markus, A., Alves, F., Salditt, T., 2019. Contrast enhancement for visualizing neuronal cytoarchitecture by propagation-based X-ray phase-contrast tomography. *NeuroImage* 199, 70–80. <https://doi.org/10.1016/j.neuroimage.2019.05.043>.
- Töpperwien, M., van der Meer, F., Stadelmann, C., Salditt, T., 2020. Correlative X-ray phase-contrast tomography and histology of human brain tissue affected by Alzheimer's disease. *NeuroImage* 210, 116523. <https://doi.org/10.1016/j.neuroimage.2020.116523>.
- Uludag, K., Roebroek, A., 2014. General overview on the merits of multimodal neuroimaging data fusion. *NeuroImage* 102, 3–10. <https://doi.org/10.1016/j.neuroimage.2014.05.018>.
- Vågberg, W., Persson, J., Szekely, L., Hertz, H.M., 2018. Cellular-resolution 3D virtual histology of human coronary arteries using X-ray phase tomography. *Sci. Rep.* 8 (1), 11014. <https://doi.org/10.1038/s41598-018-29344-3>.
- Vescovi, R., Du, M., de Andrade, V., Scullin, W., Gürsoy, D., Jacobsen, C., 2018. Tomosaic: efficient acquisition and reconstruction of teravoxel tomography data using limited-size synchrotron X-ray beams. *J. Synchrotron Radiat.* 25 (5), 1478–1489. <https://doi.org/10.1107/S1600577518010093>.
- Vo, N.T., Atwood, R.C., Drakopoulos, M., 2018. Superior techniques for eliminating ring artifacts in X-ray micro-tomography. *Opt. Express* 26 (22), 28396–28412. <https://doi.org/10.1364/OE.26.028396>.
- Wehrli, H., Bezrukov, I., Wiehr, S., Lehnhoff, M., Fuchs, K., Mannheim, J., Quintanilla-Martinez, L., Kohlhofer, U., Kneilling, M., Pichler, B., Sauter, A., 2015. Assessment of murine brain tissue shrinkage caused by different histological fixatives using magnetic resonance and computed tomography imaging. *Histol. Histopathol.* 30, 601–613. <https://doi.org/10.14670/HH-30.601>.
- Weitkamp, T., Scheel, M., Giorgetta, J., Joyet, V., Roux, V.L., Cauchon, G., Moreno, T., Polack, F., Thompson, A., Samama, J., 2017. The tomography beamline ANATOMIX at Synchrotron SOLEIL. *J. Phys. Conf. Ser.* 849, 012037 <https://doi.org/10.1088/1742-6596/849/1/012037>.
- Wolfe, D., 2019. 6 – tissue processing. In: Suvarna, S.K., Layton, C., Bancroft, J.D. (Eds.), *Bancroft's Theory and Practice of Histological Techniques*, eighth ed. Elsevier, pp. 73–83.
- Zdora, M.-C., Thibault, P., Kuo, W., Fernandez, V., Deyhle, H., Vila-Comamala, J., Olbinado, M.P., Rack, A., Lackie, P.M., Katsamenis, O.L., Lawson, M.J., Kurtcuoglu, V., Rau, C., Pfeiffer, F., Zanette, I., 2020. X-ray phase tomography with near-field speckles for three-dimensional virtual histology. *Optica* 7 (9), 1221–1227. <https://doi.org/10.1364/OPTICA.399421>.
- Zhang, M., Zhou, L., Deng, Q.-F., Yuan Xie, Y., Xiao, T., Cao, Y., Zhang, J., Chen, X.-M., Zhen Yin, X., Xiao, B., 2015. Ultra-high-resolution 3D digitalized imaging of the cerebral angioarchitecture in rats using synchrotron radiation. *Sci. Rep.* 5, 14982. <https://doi.org/10.1038/srep14982>.